Fuel 277 (2020) 118197

Contents lists available at ScienceDirect

Fuel

journal homepage: www.elsevier.com/locate/fuel

Full Length Article

Empirical correlation for spray half cone angle in plain-jet airblast atomizers

András Urbán[a], Bálint Katona[a], Milan Malý[b], Jan Jedelský[b], Viktor Józsa[a,*]

[a] Budapest University of Technology and Economics, Faculty of Mechanical Engineering, Department of Energy Engineering, 1111, Budapest, Műegyetem rkp. 3., Hungary
[b] Faculty of Mechanical Engineering, Brno University of Technology, Technicka 2896/2, 616 69 Brno, Czech Republic

ARTICLE INFO

Keywords:
Airblast
Rapeseed oil
Spray cone angle
Image processing
Threshold
Atomization

ABSTRACT

Plain-jet airblast atomizers are widely used in industrial applications. The literature contains numerous papers on Sauter mean diameter, however, there is no estimation method available for spray cone angle, *SCA*, which derivation is the primary goal of this study. Four distinct, practical model liquids were analyzed: distilled water, diesel oil, light heating oil, and crude rapeseed oil. The atomizing pressure and liquid preheating temperature were varied in the range of 0.3–2.4 bar and 25–85 °C, respectively. This latter parameter enabled a wide and continuous liquid kinematic viscosity investigation range of 0.33–44.2 mm^2/s. The resulting sprays were imaged at various shutter speeds for proper edge detection. An adaptive thresholding algorithm was developed in Matlab software environment to calculate *SCA*. The methodology is discussed in detail to facilitate the re-implementation of this technique since there is no generally accepted method for *SCA* measurement. *SCA* inversely varied with liquid density and followed a power law with the air-to-liquid mass flow ratio; however, the derived expression also performed well by replacing air-to-liquid mass flow ratio by either Mach number or momentum flux ratio. A simple empirical equation was derived, which allows the estimation of *SCA* of airblast atomization in a wide parameter range within a 3.5% deviation. The measured results were evaluated in the light of high-speed camera images in the vicinity of the nozzle; it was found that increased liquid jet breakup length decreases *SCA* while intense ligament formation increases it.

1. Introduction

The most important parameter of a liquid spray is its mean droplet size, which determines the average evaporation/solidification time, impingement, and the general interaction with the surrounding gas flow. The second highlighted parameter is the Spray Cone Angle, *SCA*, which characterizes spray spreading. It bears an emphasized role in numerous applications, including cooling [1], metallurgy [2], and combustion systems [3]. While there are a few internationally accepted and used mean droplet diameter definitions – depending on the application and focus –, there is no general definition for *SCA* [4]. A reason for it is the wide variety of existing atomizer geometries and operating conditions. Practical atomizers work in a turbulent flow field that couples with the droplet movement [5]. *SCA* determination for swirl atomizers shows a high sensitivity on the atomizer constant [6], and analytical approximations are available for inviscid flow [7]. The literature is significantly thinner for other atomizer types in which *SCA* is determined by the resulting spray instead of a well-localized liquid sheet. Hence, the droplet-turbulence interaction makes spray edge detection a nontrivial task [8]. Upon defining the edges, *SCA* can be easily estimated.

A general recommendation for *SCA* measurement of gasoline fuel injectors was made by Hung et al. [9], including spray edge determination. They have highlighted that the spray can be curved, hence a well-defined distance from the nozzle should be set. Nevertheless, their results cannot be generalized to airblast atomizers, which is the subject of this paper due to the well-established geometry ranges and specifications in reciprocating engine applications. As a consequence, 60 times the liquid orifice diameter was chosen for the present analysis that is used for pressure atomizers [4] and lies in the self-similar region of annular jets [10]. The spray edge detection can be performed by either imaging [11] or non-imaging optical techniques [12]. The image resolution of current commercial cameras is high enough to perform accurate measurements, also used in the current study. Martínez-Galván et al. [1] and Bizjan et al. [13] similarly faced the blurry spray edge problem and used a thresholding technique. Their idea was improved in the present study, i.e., by using an adaptive approach, discussed in Subsection 2.2. A similar algorithm was successfully applied in particle detection in microscopy [14] and X-ray image processing [15]. Since a spray image is an instantaneous map of droplets, averaging is necessary to eliminate this variation. It can be done by averaging a certain number of images [1] or using a proper exposure time. In the present

* Corresponding author.
E-mail address: jozsa@energia.bme.hu (V. Józsa).

https://doi.org/10.1016/j.fuel.2020.118197
Received 29 February 2020; Received in revised form 14 April 2020; Accepted 22 May 2020
Available online 31 May 2020

Nomenclature

Latin letters

A	[deg] constant in the *SCA* correlation
a	[m/s] speed of sound
$ALR = \dot{m}_A/\dot{m}_L$	[–] air-to-liquid mass flow ratio
B	[–] constant in the *SCA* correlation
d_0	[mm] liquid pipe inner diameter of the atomizer
$\dot{m}$	[kg/s] mass flow rate
$\mathrm{Ma} = w/a$	[–] Mach number
$MFR = \rho_A \cdot w_A^2/\rho_L \cdot w_L^2$	[–] momentum flux ratio
N_1, N_2	[–] non-dimensional numbers
$\mathrm{Oh} = \sqrt{\mathrm{We}}/\mathrm{Re}$	[–] Ohnesorge number
p	[bar] pressure
R	[J/(kg·K)] specific gas constant
R^2	[–] coefficient of determination
$\mathrm{Re} = w_R \cdot d_0/\nu$	[–] Reynolds number
$S_{r,A}$	[–] relative standard deviation of A constant
SCA	[deg] spray cone angle
SMD	[μm] Sauter mean diameter
T	[°C] temperature
w	[m/s] velocity
$\mathrm{We} = \rho \cdot w_R^2 \cdot d_0/\sigma$	[–] Weber number

Greek letters

κ	[–] specific heat ratio
μ	[kg/(m·s)] dynamic viscosity
ν	[m^2/s] kinematic viscosity
ρ	[kg/m^3] density
σ	[N/m] surface tension
0	ambient
25 °C	at 25 °C
A	atomizing air
g	atomizing air gauge
L	liquid
R	relative

Abbreviations

D	diesel oil
LHO	light heating oil
RO	crude rapeseed oil
SSE	sum of squared estimate of errors
W	distilled water
.	Tilde denotes non-dimensional numbers derived from a single physical quantity.

paper, this latter method was used, with an extension of evaluating the *SCA* variation with the shutter speed.

Airblast atomizers were developed to replace pressure swirl atomizers, which have low flexibility in the liquid flow rate [16]. Turndown ratio of 50:1 was made available through governing the atomization process by the high-velocity airflow; the liquid is injected at a few m/s without lower limitation. This atomizer type belongs to the twin-fluid family and relies on the available high-pressure gas, which blows over the liquid surface, leading to ligament then droplet formation; the governing physics was reviewed by Lasheras and Hopfinger [17]. The presently investigated plain-jet airblast atomizer has a simple pipe-in-pipe design that makes its manufacturing and maintenance easy. Spray characteristics of airblast atomization were investigated by Ma et al. [18] and Gad et al. [19]; nevertheless, they did not aim to derive an empirical correlation between the operating parameters and *SCA* which is the primary goal of this study. Tareq et al. [20] investigated the *SCA* of a prefilming airblast atomizer, and, similarly, they did not derive any correlation for this parameter.

The liquid breakup process governs *SCA*, hence, the liquid disintegration in the vicinity of the nozzle greatly affects the final result. Watanawanyoo et al. [21] investigated a twin-fluid atomizer in a similar air-to-liquid parameter range, which is analyzed presently, detailed in Subsection 2.1. They identified various breakup modes and estimated only the droplet size distribution 100 mm downstream of the nozzle without *SCA* evaluation. Charalampous et al. [22] analyzed the liquid jet breakup length by three different techniques, concluding that even a simple electrical connectivity technique can lead to significant results; however, it requires an intrusive probe. The liquid jet breakup length affects the spray spreading since the high-velocity air jet quickly decays as it interacts with the low-velocity liquid jet. Hence, greater liquid jet breakup length leads so smaller *SCA*. A novel, dual-angle particle tracking velocimetry technique for spray and droplet breakup measurement was proposed by Pham et al. [23], which enables highly detailed tracking of the droplet breakup process.

If numerous parameters influence a quantity, the use of the Buckingham π theorem helps in finding the proper correlation through deriving non-dimensional quantities [24]. The absence of such an investigation for *SCA* of airblast atomizers starts with the analysis of the possible parameters affecting atomization, which are discussed in detail for, e.g., determining the Sauter Mean Diameter, *SMD* [25]. An early work by Abramovich [26] on pressure atomization concluded that *SCA* depends on the density ratio of air and liquid. Ultimately, it was found that Ohnesorge and Weber numbers determine the atomization mode, hence *SCA* is also affected by them [4]. This paper is a successor of our previous work in which the *SMD* of the spray was deeply investigated [27]. The presently investigated liquids are the same for consistency: distilled water (W), standard diesel oil (D, EN 590), light heating oil (LHO), and crude rapeseed oil (RO).

The novelty of the present paper is principally filling a scientific gap by deriving an empirical correlation for *SCA* of a plain-jet airblast atomizer. Since the droplet formation is largely depending on the near-nozzle regime of the spray, the liquid structures of the primary breakup are visually evaluated. The third goal is to provide a general *SCA* determining framework to make this procedure transparent and easy to implement to practical applications where measurement techniques beyond a commercial digital camera are seldom available.

2. Materials and methods

Firstly, the experimental setup is detailed, along with the discussion of the measurement uncertainties. Then the image processing methodology is described to provide a general framework for *SCA* analysis for a possible re-implementation of this technique. Lastly, the derivation of the non-dimensional quantities and the empirical correlation for *SCA* are detailed.

2.1. Experimental setup

The schematic drawing of the atomization test rig shown in Fig. 1a, featuring the nozzle tip. The liquid jet was introduced to the plain-jet airblast atomizer via a central pipe with 0.4 mm inner diameter while inner and outer diameters of the annular atomizing air orifice were 0.8 mm and 1.6 mm, respectively. The gauge pressure of the atomizing air, p_g, was set by a regulator valve in the range of 0.3 and 2.4 bar in 5 steps with 1 kPa accuracy. The air was also used to pressurize the liquid tank to maintain a low yet smooth liquid flow rate which was 0.35 g/s for all the four liquids: D, LHO, RO, and W. The liquid volume flow rate was measured by an Omega FPD3202 flow meter which has $<$ 2.7%

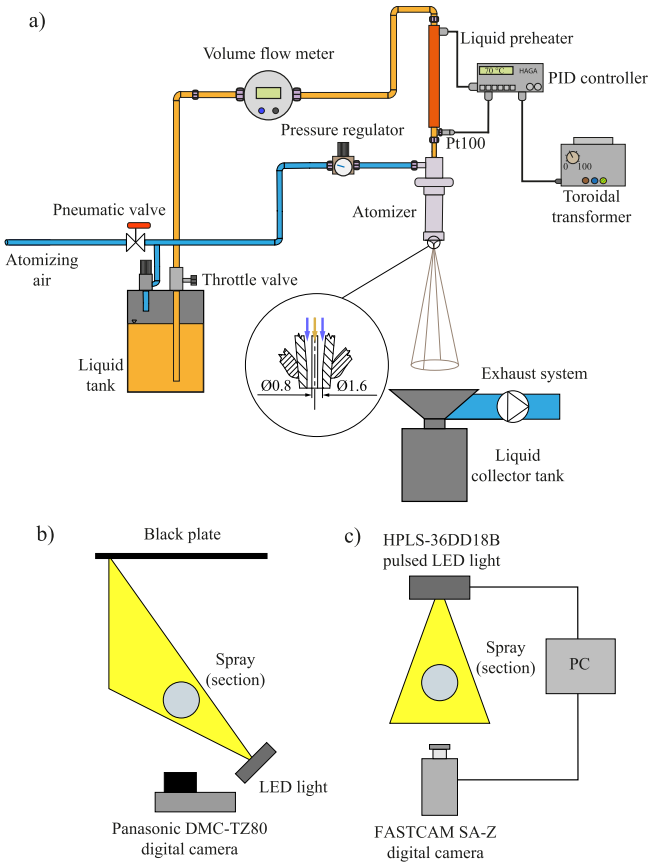

Fig. 1. Schematic of a) liquid and atomizing air piping and their instrumentation and optical setup of b) *SCA* and c) primary breakup measurement.

uncertainty at 95% level of significance. The calibration was performed at six points around the desired flow rate, using the setup presented in Fig. 1. An electric heater was installed to the liquid line to set the preheating temperature, T_L, between 25 and 85 °C in five 15 °C steps. The liquid temperature was controlled by a PID controller, using a B class Pt100 resistance thermometer with an accuracy of < 0.8 °C. The conditions listed above resulted in 100 different conditions in total with a wide parameter range in surface tension (20.7–32.1 and 62.3–72.1 mN/m), kinematic viscosity (0.33–44.2 mm^2/s), and liquid density (808–997 kg/m^3), which are characteristic for liquid fuels in combustion. Note that the gap in surface tension is present due to the significantly higher values for water than other hydrocarbon liquids. Nevertheless, the principal aim in selecting the liquids was to ensure a continuous range in viscosity. The measured material properties, along with their corresponding uncertainties, are discussed in our previous work [27]. A fan was used to remove the mist to enable the acquisition of clear images without affecting the *SCA*. It did not work flawlessly at high p_g when very fine spray was generated, discussed in Subsection 2.2. The range of the key non-dimensional numbers is summarized in Table 1 in Subsection 2.3.

The shutter speed was expected to affect *SCA* as longer exposure time allows more information to be collected in the peripheral regime where the droplet mass flux is low there. Hence, 1/60 s, 1/80 s, and 1/100 s shutter speeds were used to get relatively sharp images. Five pictures were recorded with all three settings, which means 1500 images in total to be processed. The conversion factor in these images was 15.5 pixels/mm. The spray was imaged in front of a black plate by a Panasonic DMC-TZ80 commercial digital camera and illuminated from the front in a small angle by a commercial 50 W LED spotlight, shown in Fig. 1b. The image resolution was 18 MP, while the focal ratio was set to 4.3. Since airblast atomization generates dilute spray, the position of the LED light had no notable influence on the calculated *SCA* values, which was carefully checked.

In order to understand the droplet formation and *SCA* variation better, a high-speed camera, a FASTCAM SA-Z type 2100 K-M − 16 GB (Photron, Japan) with long-distance microscope 12X Zoom lens (NAVITAR, USA) composed of 2X F-mount adapter (type 1–62922), 12 mm F.F zoom lens (type 1–50486) and attached 0.25X lens (type 1–50011), was used to capture the breakup of the liquid jet in the vicinity of the atomizer nozzle; the optical setup is shown in Fig. 1c. The spray was illuminated from the background by an HPLS-36DD18B (Lightspeed Technologies, Inc., USA) pulsed LED light source. The light pulse duration was 100 ns. Note that the recording of these images was performed earlier, along with the Phase Doppler measurements in ref [27], using the same atomizer and liquid preheater apparatus. The difference was that the maximum T_L was higher than the presently set 85 °C value. Hence, T_L was 90 °C for W and 100 °C for the three other liquids for high-speed imaging results. The shutter speed was 1/630,000 s or 159 s, and the frame rate was 160,000 frames/second. The image resolution was 256 × 256 pixels, which is equivalent to 3.2 × 3.2 mm physical size with a conversion factor of 80 pixels/mm. The high frame rate was necessary to capture the movement of the fluid packets while the atomizing discharge velocity was in the range of 208–420 m/s, according to p_g = 0.3–2.4 bar. Since the high-speed camera was focused on the vicinity of the nozzle, *SCA* cannot be deduced from these results. Nevertheless, the droplet formation and their motion due to turbulence allow a better understanding of the variation of *SCA*.

2.2. Image processing

To process a large number of images without the bias of manual evaluation, a Matlab code was developed for this purpose. Its flow chart is shown in Fig. 2. Since the elementary processes are simple manipulation algorithms, the runtime is in the range of one second.

The first step is reading the image to be processed. Then the image has to be cut to a uniform shape, which is crucial for the evaluation, shown in Fig. 3a. Pre-calibration is required for cropping, i.e., the pixels are converted to physical dimensions. The outlet diameter of the liquid jet is 400 μm, being equal to the inner diameter of the fuel pipe. It was considered as a reference for image calibration, also supported by the high-speed images focusing on the primary breakup region, discussed in Subsection 3.2. Next, the resulting image was subjected to gamma correction and grayscale conversion, shown in Fig. 3b. Gamma between 0 and 1 makes the image lighter while values exceeding one shifts it towards black. A constant value of 1.1 was used in the present study to remove a portion of the visible fine mist and image noise, based on the following observations. Generally, excessive gamma values affect *SCA*,

Table 1
The main non-dimensional range of the liquids.

		D	LHO	RO	W
p_g [bar]	min.	0.3	0.3	0.3	0.3
	max.	2.4	2.4	2.4	2.4
ALR [-]	min.	0.78	0.78	0.78	0.78
	max.	2.07	2.07	2.07	2.07
Re_A [-]	min.	9166	9173	9178	9192
	max.	30,712	30,723	30,734	30,751
$Re_L/10^6$ [-]	min.	22.7	5.04	1.57	91.2
	max.	115.4	51.8	21.0	380
We_A [-]	min.	824.7	711.4	659.2	294.4
	max.	5582	5080	4375	1859
Oh_L [-]	min.	0.014	0.0309	0.072	0.00274
	max.	0.0325	0.140	0.442	0.00528
Ma [-]	min.	0.62	0.62	0.62	0.62
	max.	1.45	1.45	1.45	1.45
MFR [-]	min.	5.71	5.96	6.19	6.86
	max.	30.73	32.05	32.31	36.9

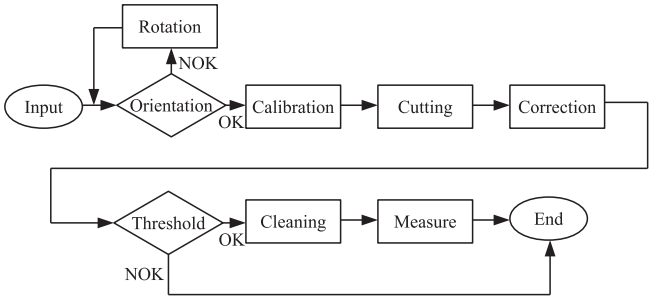

Fig. 2. The image processing flow chart.

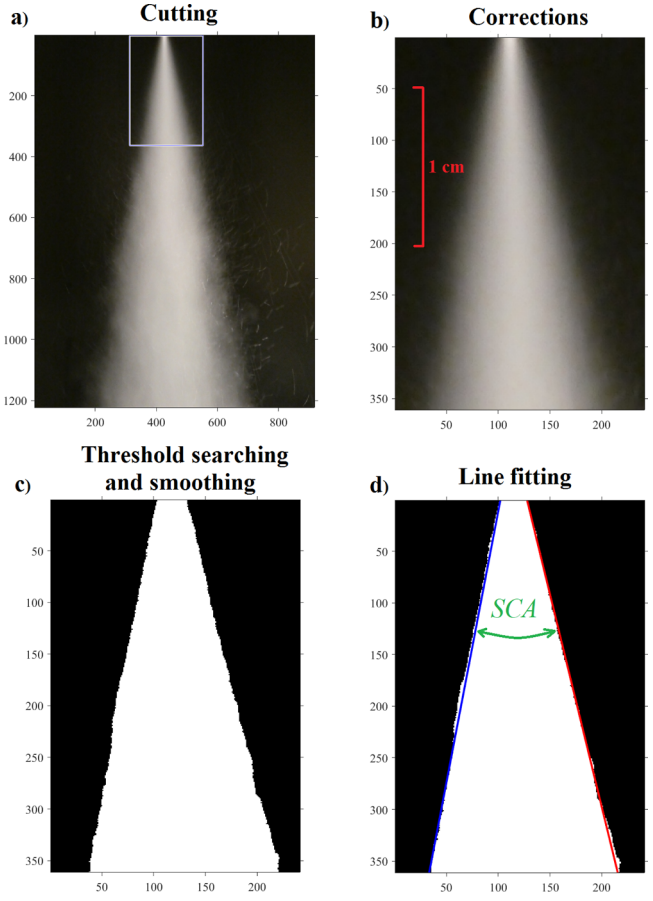

Fig. 3. The steps of image processing and *SCA* determination. The axes show the number of pixels.

which should be avoided. This effect was observed at, e.g., $p_g = 2.4$ bar when fine spray was generated and the mist became dense, making the edge detection cumbersome. Higher viscosity cases also caused biased results when excessive gamma correction was applied. Then the image was subjected to binary conversion where 1 is the white an 0 is the black. This procedure was necessary to prepare the thresholding algorithm to calculate the boundaries of the spray. Final smoothing was performed to fill the inner gaps, shown in Fig. 3c. By searching for the first and last white pixels in a row, the spray boundaries can be determined, resulting in two curves. Fig. 3d shows the fitted lines to the left and right edge of the spray boundary, which intersection angle gives the *SCA* ultimately.

Besides the shutter speed selection, inappropriate threshold value leads to biased results. Hence, sweeping with the threshold level was performed first, shown in Fig. 4, to adaptively find the appropriate threshold. Initially, a small value does not affect the number of white pixels. Above 0.8 here, only black pixels remain since there was no fully white pixel. Even though a black background was used, the corresponding part of the image was dark grey in the images. Hence, the initial rapid decrease is due to the conversion of the background to black. Then smaller, lighter patches of the image turn to black that precedes the disappearing of the substantial parts of the spray, shown in Fig. 4b, as a local minimum before the jump to zero. To find the spray edges, this minimum was calculated, which adaptively provided the appropriate threshold value for *SCA* determination. Hence, no single threshold value was used in the present study, unlike in the case of Gamma. Even though there was a difference in the shutter speeds, the applied procedure resulted in highly similar results, and the discussed *SCA* value in Subsection 3.1 was the average of them. Note that the variation of the *SCA* values was very low, hence the averaging marginally affected the final result.

High p_g resulted in droplets below 5 μm, which were less prone to leave the test section due to their low inertia, shown in Fig. 5. To avoid biased *SCA* determination, excessive mist suction should be avoided that inevitably results in coarse image quality. As a consequence, a manual review of the filtering procedure was necessary at a few operating points.

2.3. Empirical equation formulation

By performing the Buckingham π theorem on the relevant parameters in the present measurement series and, the following non-dimensional numbers were derived. Firstly, the single physical quantity ratios – and also their reciprocals – can be considered:

$$\tilde{T_A} = (T_A + 273.15)/(T_L + 273.15) \quad (1)$$

$$\tilde{T_L} = 25^{\circ}\mathrm{C}/T_L \quad (2)$$

$$\tilde{\rho_A} = \rho_A/\rho_L \quad (3)$$

$$\tilde{\rho}_L = \rho_{L,25^{\circ}\mathrm{C}}/\rho_L \quad (4)$$

$$\tilde{\nu}_A = \nu_A/\nu_L \quad (5)$$

$$\tilde{\nu}_L = \nu_{L,25^{\circ}\mathrm{C}}/\nu_L \quad (6)$$

$$\tilde{\mu}_A = \mu_A/\mu_L = \nu_A{\cdot}\rho_A/(\nu_L{\cdot}\rho_L) \quad (7)$$

$$\tilde{\mu_L} = \mu_{L,25^{\circ}C}/\mu_L = \nu_{L,25^{\circ}C}{\cdot}\rho_{L,25^{\circ}C}/(\nu_L{\cdot}\rho_L) \quad (8)$$

$$\tilde{\sigma} = \sigma_{25^{\circ}\mathrm{C}}/\sigma \quad (9)$$

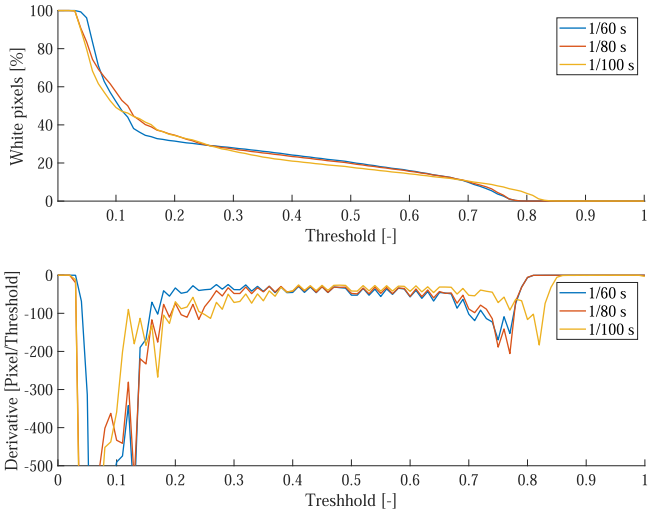

Fig. 4. Image thresholding. a) percentage of white pixels and b) derivative of a).

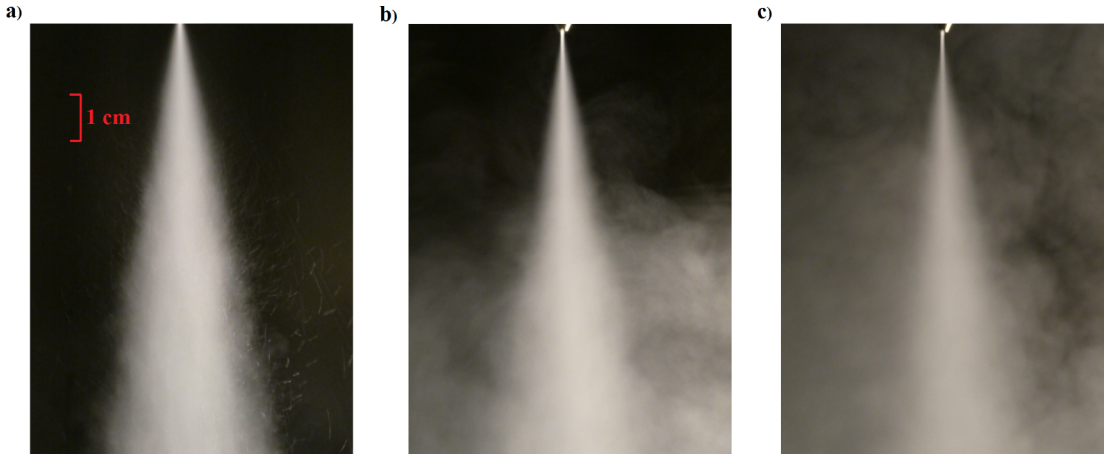

Fig. 5. Raw images of D atomization at $T_L = 25$ °C and $p_g =$ a) 0.3 bar, b) 0.9 bar, c) 2.4 bar. Note the coarsening image quality.

$$ALR = \dot{m}_A/\dot{m}_L \tag{10}$$

$$\mathrm{Ma} = w_A/a \tag{11}$$

where T is the temperature, ρ is the density, ν is the kinematic viscosity, μ is the dynamic viscosity, σ is the surface tension, ALR is the air-to-liquid mass flow ratio, $\dot{m}$ is the mass flow rate, Ma is the Mach number, a is the local speed of sound, and w_A is the air velocity after adiabatic expansion [27]. Tilde denotes non-dimensional numbers derived from a single physical quantity. Subscript 25 °C refers to at 25 °C. a, w_A, and ρ_A are calculated by Eqs. (12)–(14):

$$a = \sqrt{R\cdot\kappa\cdot(T_A + 273.15)} \tag{12}$$

$$w_A = \sqrt{\frac{2\cdot\kappa}{\kappa-1}\cdot R\cdot(T_{A,0}+273.15)\cdot\left[1-\left(\frac{p_A}{p_A+p_g}\right)^{\frac{\kappa-1}{\kappa}}\right]} \tag{13}$$

$$\rho_A = \frac{p_A+p_g}{R\cdot(T_{A,0}+273.15)}\cdot\left(\frac{p_A}{p_A+p_g}\right)^{\frac{1}{\kappa}} \tag{14}$$

where $R = 287$ J/(kg·K) is the specific gas constant of air, $\kappa = 1.4$ is the

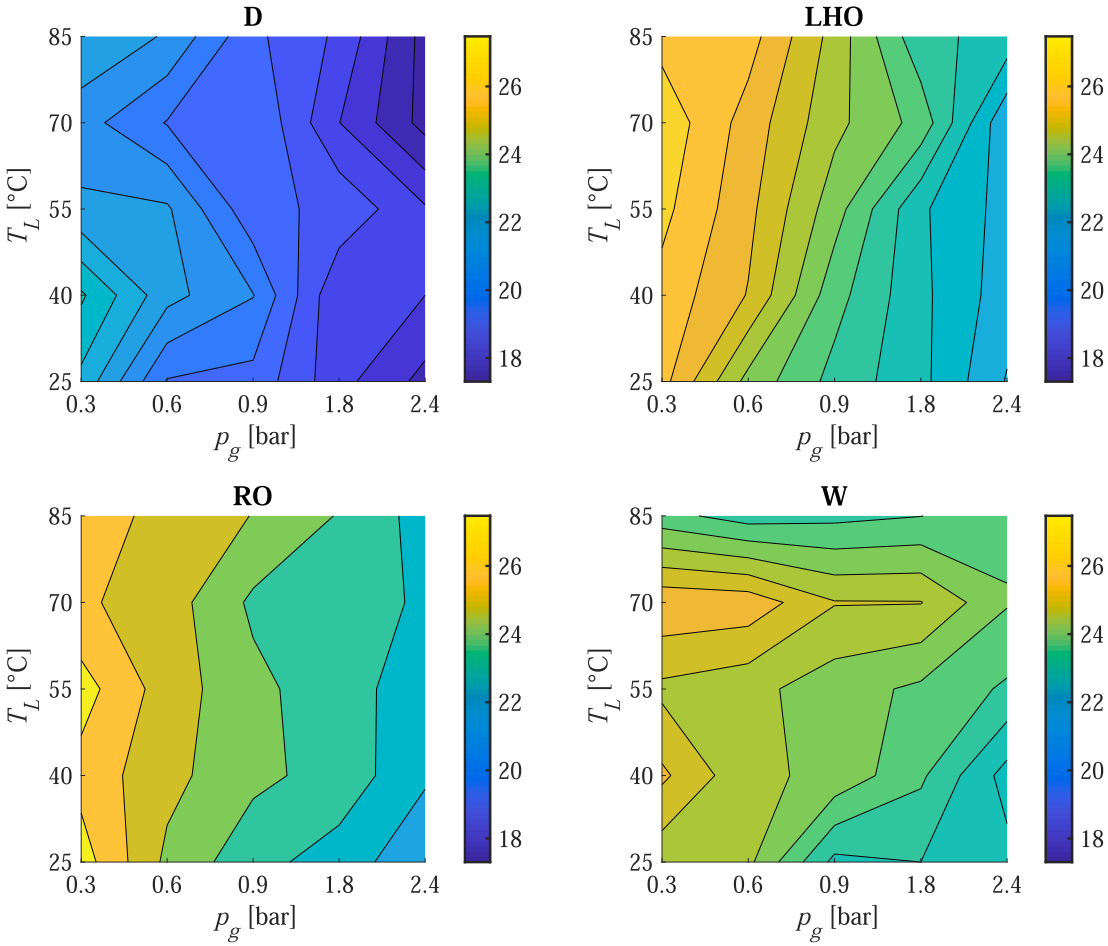

Fig. 6. *SCA* as a function of T_L at various p_g for all liquids.

specific heat ratio, p_A is the ambient pressure, which is also the atomizing air pressure after the adiabatic expansion. $T_{A,0}$ is the atomizing air temperature before reaching the nozzle. Subscript A refers to atomizing air – after the expansion –, L denotes liquid, and $T_{A,0}$ is the atomizing air temperature before the nozzle. Equations (2), (4), (6), and (8) were introduced to allow the isolated inclusion of liquid temperature without affecting the quantities which contain the properties of atomizing air. Besides the single quantity ratios, three further highly relevant non-dimensional numbers in sprays were also evaluated, shown by Eqs. (15)–(18):

$$\mathrm{Re} = w_R \cdot d_0 / \nu \tag{15}$$

$$\mathrm{We} = \rho \cdot w_R^2 \cdot d_0 / \sigma \tag{16}$$

$$\mathrm{Oh} = \sqrt{\mathrm{We}}/\mathrm{Re} = \mu / \sqrt{\rho \cdot d_0 \cdot \sigma} \tag{17}$$

$$MFR = \rho_A \cdot w_A^2 / \rho_L \cdot w_L^2 \tag{18}$$

where Re is the Reynolds number, We is the Weber number, Oh is the Ohnesorge number, and *MFR* is the momentum flux ratio. $w_R = w_A - w_L$ is the relative velocity between the two streams and σ is the surface tension. Since both density and viscosity can be understood as the

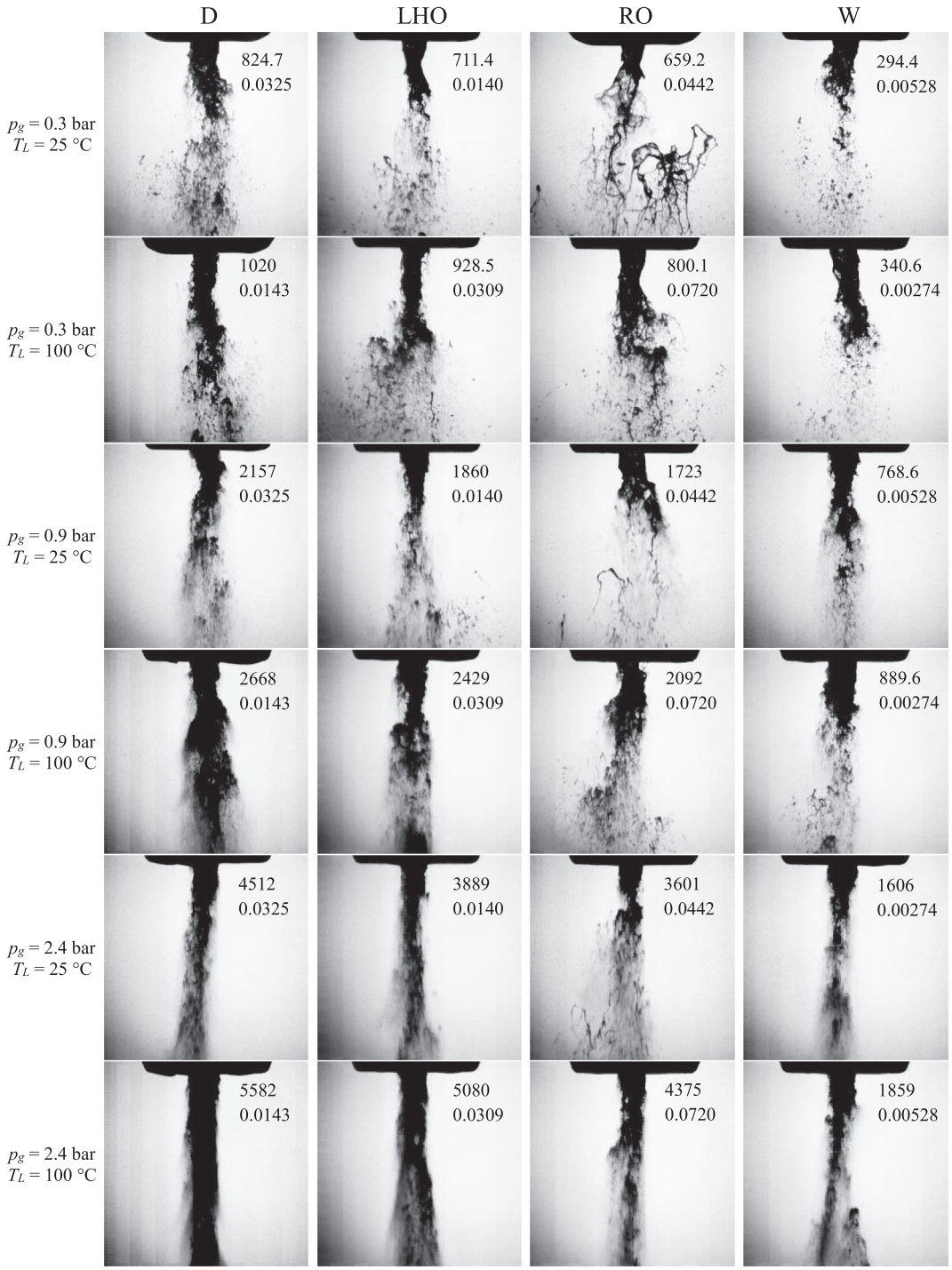

Fig. 7. High-speed images in the vicinity of the nozzle of all liquids and various p_g and T_L. Note that the upper limit of T_L was 90 °C in the case of W instead of 100 °C. The physical size of the images is 3.2 × 3.2 mm. The numbers in the top right corner are We_A and Oh.

Table 2
Performance of various non-dimensional numbers at N_2 while $N_1 = \tilde{\rho}_L$ was used. Note that the considered dataset of W was limited to $T_L = 70$ °C.

N_2	Liquid	R^2	*SSE*	$S_{r,A}$
ALR	D	0.920	8.24	0.0225
	LHO	0.950	4.24	0.00760
	RO	0.951	5.9	0.0198
	W	0.881	7.46	0.0185
Ma	D	0.912	8.08	0.0183
	LHO	0.941	13.4	0.00378
	RO	0.961	14.3	0.0117
	W	0.864	13.5	0.0203
MFR	D	0.912	9.06	0.0633
	LHO	0.937	15.6	0.0309
	RO	0.948	16.2	0.0779
	W	0.848	12.7	0.0443
$\tilde{\rho}_A$	D	0.933	17.7	1.099
	LHO	0.960	48.1	0.447
	RO	0.937	68.1	0.958
	W	0.895	52.4	0.553
We_L	D	0.899	11.9	0.155
	LHO	0.926	11.2	0
	RO	0.945	193	0.363
	W	0.835	61.9	0.260
Re_A	D	0.930	9.47	0.228
	LHO	0.951	4.29	0.0729
	RO	0.949	8.33	0.151
	W	0.862	37.3	0.231
Re_L	D	0.903	856	0
	LHO	0.930	117	0.000134
	RO	0.946	150	0
	W	0.836	15.4	0
$\tilde{T}_A$	D	0.943	27.1	0.0492
	LHO	0.960	221	0.0465
	RO	0.937	180	0.0269
	W	0.894	13.9	0.0339

material property of either the atomizing air or the liquid, the first three of these numbers also feature *A* or *L* subscript in the following for clarification. The main non-dimensional parameters of the present investigation are listed in Table 1. p_g, *ALR*, Re_A, Ma, and *MFR* are identical or similar for all liquids. Since the surface tension of W is about the triple of that of the other liquids, leading to differences in We_A. Re_L and Oh include the liquid viscosity, which was carefully selected to allow the investigation of a continuous range. Hence, the range of these properties is unique for all liquids.

Based on all the non-dimensional numbers, it is evident that keeping all of them similar is impossible. To overcome this issue and allow the comparison of various atomizers and liquid sprays, Ohnesorge introduced the Oh-Re_L diagram [4] in which all of the points lie in the 'atomization' range. Faeth et al. [28] investigated the breakup regimes of droplets and introduced a We_A-Oh diagram for classification. Presently, all the points fall into the 'shear breakup' regime since $We_A > 200$ and $Oh < 0.5$. Consequently, it can be stated that the droplet formation is governed by the same physical mechanisms in all of the above cases, hence liquid breakup and *SCA* of different liquids at different conditions can be compared.

3. Results and discussion

Firstly, the *SCA* measurement results are presented, evaluating the effect of all p_g, T_L, and liquids. Since the jet breakup has a significant impact on *SCA*, the primary breakup is analyzed next at two temperatures and three pressure for all liquids to better understand the above results. Lastly, the derivation of the empirical correlation is detailed, using an optimization algorithm. Since the parameter fitting easily results in high R^2 values, the fitted coefficients were perturbed by 1% to see their effect on the sum of the squared estimate of errors, *SSE*, to find the results with low sensitivity and hence potentially applicable for *SCA* estimation.

Table 3
Poorly performed combinations in the case of D.

N_1	N_2	R^2	*SSE*	$S_{r,A}$
$\tilde{\rho}_L$	$\tilde{\nu}_A$	0.873	2.3×10^9	0.641
$\tilde{\rho}_L$	$\tilde{\mu}_A$	0.570	214,415	1.86
$\tilde{\rho}_L$	We_A	0.915	1128	0.154
Oh_L	*ALR*	0.749	995	0.294
Oh_L	Ma	0.915	995	0.293
Oh_L	*MFR*	0.913	991	0.298
$\tilde{T}_L$	*ALR*	0.546	2598	0.521
$\tilde{T}_L$	Ma	0.556	2599	0.517
$\tilde{T}_L$	*MFR*	0.589	1980	0.540
$\tilde{\nu}_L$	*ALR*	0.922	1463	0.390
$\tilde{\nu}_L$	Ma	0.911	9017	0.0183
$\tilde{\nu}_L$	*MFR*	0.911	9695	0.0633
$\tilde{\mu}_L$	*ALR*	0.922	8028	0.0225
$\tilde{\mu}_L$	Ma	0.911	8067	0.0183
$\tilde{\mu}_L$	*MFR*	0.911	8691	0.0633
$\tilde{\sigma}$	*ALR*	0.922	71.7	0.092
$\tilde{\sigma}$	Ma	0.911	191	0.0183
$\tilde{\sigma}$	*MFR*	0.911	244	0.063

Table 4
Increase of *SSE* in percentage compared to the original value by perturbing only *A* and *B* by ± 1% while the other constant was unchanged.

N_2	Liquid	*A* + 1%/-1%	*B* + 1%/-1%
ALR	D	15.1/8.80	0.635/0.469
ALR	LHO	45.2/24.3	1.14/1.59
ALR	RO	33.4/17.5	0.82/1.13
ALR	W	9.70/40.8	0.079/0.09
Ma	D	6.05/30.0	0.61/0.491
Ma	LHO	29.4/50.5	0.618/0.707
Ma	RO	35.7/55.7	0.654/0.732
Ma	W	21.2/38.0	0.338/0.348
MFR	D	38.5/16.3	6.47/8.60
MFR	LHO	31.3/39.2	12.6/11.0
MFR	RO	34.3/52.0	13.2/11.7
MFR	W	18.1/36.2	2.87/2.63
$\tilde{T}_A$	D	37.9/30.1	4.59/4.77
$\tilde{T}_A$	LHO	19.0/17.3	1.49/1.50
$\tilde{T}_A$	RO	20.8/18.7	1.52/1.55
$\tilde{T}_A$	W	52.3/34.5	1.61/1.63

Table 5
Constant of Eq. (20) for the investigated liquids.

N_2	Const.	D	LHO	RO	W
ALR	*A*	20.7	25.0	25.1	24.3
	B	−0.20	−0.19	−0.18	−0.07
Ma	*A*	19.5	23.6	23.8	23.8
	B	−0.23	−0.22	−0.21	−0.08
MFR	*A*	27.2	32.0	32.0	26.8
	B	−0.11	−0.11	−0.11	−0.04

3.1. SCA measurement results

The determined *SCA* as a function of p_g and T_L for all liquids is shown in Fig. 6. The results show a decreasing trend principally with increasing p_g in all the cases. It can be explained by the effect of continuously increasing the axial momentum of the atomizing air that intensifies droplet convection. Turbulence facilitates the radial propagation of droplets and counteracts with this phenomenon, which is becoming more intense with the increased p_g. However, the former effect is notably stronger, leading to ultimately smaller *SCA* at higher

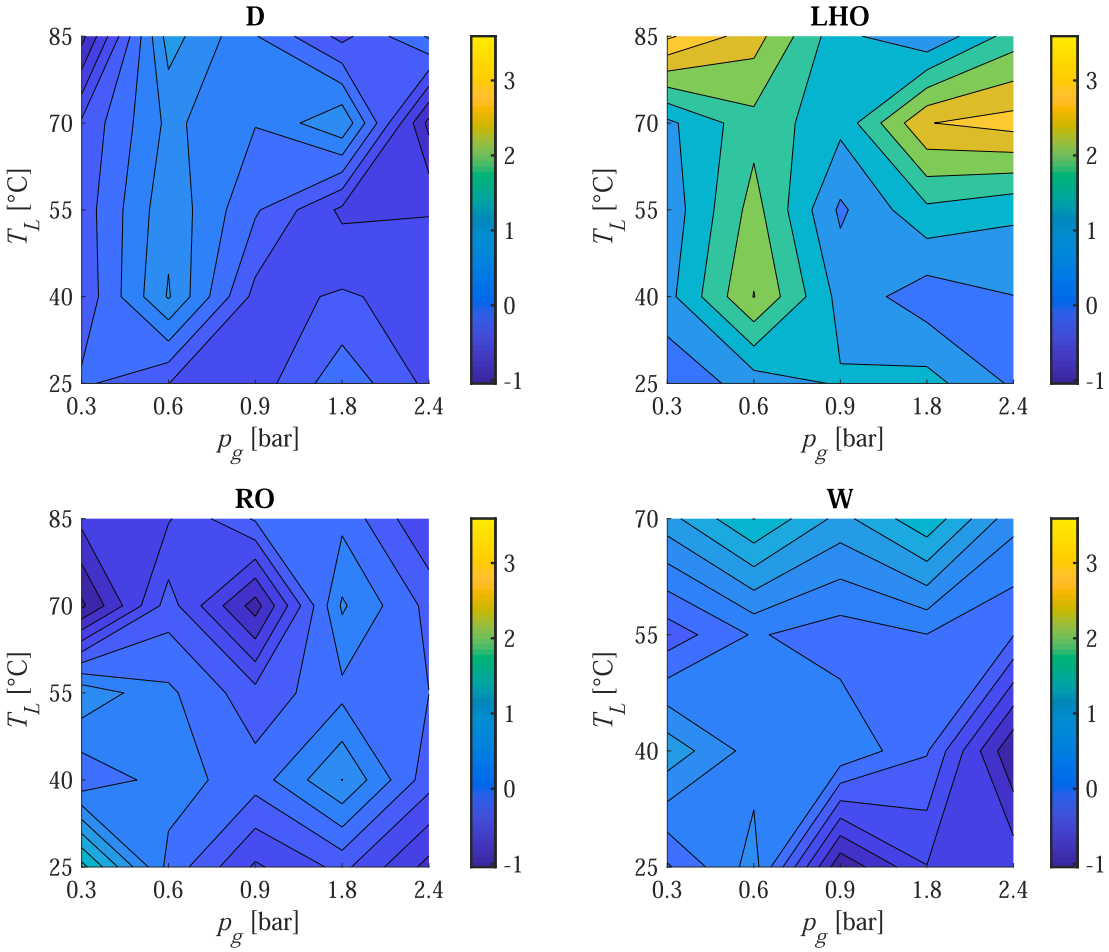

Fig. 8. The relative deviation of Eq. (20) in percentage at each measurement point.

p_g. Increased T_L features slightly increased *SCA* for principally LHO and RO. Its effect on D and W is significantly lower, complying with the limiting viscosity term, defined in our previous work [27]. It is a kinematic viscosity value below which the liquid preheating has no additional physical effect on the We-containing term of *SMD* estimation beyond the temperature-dependent material properties, and it was found to be 4.2 mm^2/s that was not reached by RO at any investigated T_L and reached by LHO at T_L = 55 °C.

The *SCA* results show that the variation in the investigated ranges is relatively small. D and LHO showed 5.27° and 5.38°, respectively, while it was 6.22° for RO, which is related to the significant drop in its viscosity with preheating, discussed in Subsection 3.2. The variation of *SCA* of W was only 3.6°. The measurement results of W at 85 °C show a decrease at all p_g, which is against the other trends, and the material properties do not justify this phenomenon. Also, this T_L is well below the boiling temperature; hence, local steam formation in the preheating chamber can be excluded. Moreover, *SCA* varied marginally with p_g unlike in the case of the other liquids and lower T_L of W atomization. Since this observation requires significantly deeper, highly focused further investigations, the measurement results of W were evaluated only up to 70 °C.

3.2. Primary jet breakup visualization

The primary breakup of liquid jets is shown in Fig. 7 at T_L = 25 and 100 °C – except for W where the upper limit was 90 °C, and at p_g = 0.3, 0.9, and 2.4 bar. The promptly expanding atomizing air is responsible for the dispersion of the droplets in the radial direction, which effect is greatly enhanced by the highly turbulent air jet that brings chaotic motion that also spreads the droplets in all directions. The total disintegration length of D jet is the greatest at all conditions, which is not accompanied by notable ligament formation. This seems the most significant difference between this and other liquid types and being the reason for smaller *SCA*, shown in Fig. 6. Since the vicinity of the nozzle has a lower droplet population, the tiny droplets are less likely to spread at a large angle. At p_g = 2.4 bar and T_L = 100 °C, D disintegration is rapid, and the transition between the liquid jet core and the fine droplets is not visible. The breakup of liquid packets is the catastrophic type for all liquids under these conditions.

Regarding liquid viscosity, density, and surface tension, LHO lies between D and RO. More specifically, its material properties at T_L = 100 °C closely match that of D at 25 °C, and LHO at 25 °C behaves similarly as RO at 100 °C [27] which is also observable in the corresponding images as the breakup mode closely matches. The difference in Oh of D at 25 °C and LHO at 100 °C is 5% while it is 12.5% in We$_A$ that also suggests a similar behavior. By comparing LHO at 25 °C and RO at 100 °C, Oh is halved and the 12.5% difference in We$_A$ remains. This result complies with the Oh-We$_A$ similarity condition proposed by Faeth et al. [28], mentioned earlier. By evaluating LHO at identical conditions to D and RO, it is characterized by moderate ligament formation, and the liquid jet breakup length also lies between the two liquids.

The ligament formation is most spectacular in the case of RO at p_g = 0.3 bar and T_L = 25 °C, where the liquid viscosity is the highest. This process is also observable at elevated pressures. Nevertheless, at T_L = 100 °C, the ligaments are only visible at p_g = 0.3 bar with significantly smaller sizes. The liquid spreading is high due to the intense ligament formation, leading to the highest *SCA* values in the

investigated parameter range. The high viscosity of RO is clearly visible since all the forming liquid fractions are significantly larger than in the case of other liquids.

The catastrophic jet breakup process is best visualized in the case of W, which also shows very small ligaments at all conditions due to the high surface tension value while viscosity is low, also meaning low Oh. The liquid packets are larger in the wake of the liquid jet, which undergoes further breakup downstream. The water droplets show more intense spreading in the vicinity of the nozzle, and the effect of T_L is low, as it was shown in Fig. 6. Even though We of W at elevated p_g matches that with the other liquids, Oh is one magnitude lower than that of D and two magnitudes lower than that of RO. This answers why its primary breakup significantly differs from that of other liquids.

SCA estimation based on the high-speed camera images is not possible since the spreading of the spray is delayed at higher p_g; only a slightly disturbed straight two-phase jet is visible. Even though the generated tiny droplets are visible, their spreading is only observable at a higher downstream distance. The images show only 8 d_0, while it was concluded based on the global spray images that 60 d_0 is a sufficient distance to have a fully developed *SCA*.

3.3. Deriving an empirical correlation for SCA

Upon determining the relevant non-dimensional numbers, discussed in Subsection 2.3, the formulation of the empirical correlation is the next task. Since two principal parameters were varied, p_g and T_L, the final *SCA* formula is about to be determined in the form of Eq. (19):

$$SCA = A \cdot N_1 \cdot N_2^B \tag{19}$$

where A and B are constants, and N_1 and N_2 are wildcard non-dimensional numbers. This form was derived by analyzing the *SCA* correlations for other atomizer types [4] and considering the power law effect of p_g on *SCA*, which is represented by N_2. N_1 stands for the inclusion of the effect of liquid preheating. Since the number of constants is equal to the number of varying parameters, other formulae with more degree of freedom would lead to overfitting. This extension is only could be done if the number of parameters is increasing, e.g., by adjusting the atomizer geometry, liquid mass flow rate, etc., which would lead to an excessive number of measurement points. To overcome this issue, the design of experiments method can be used, which was successfully applied by Chen et al. [29] for *SMD* determination. However, this technique only can work efficiently if the shape of the equation is well-established; hence this paper only aims to provide an adequately shaped formula, and its extension is the next step in this research.

Firstly, an R^2 analysis was performed, substituting N_1 with $\tilde{T}_L$, $\tilde{\rho}_L$, $\tilde{\nu}_L$, $\tilde{\mu}_L$, $\tilde{\sigma}$, and Oh and N_2 with $\tilde{T}_A$, $\tilde{\rho}_A$, $\tilde{\nu}_A$, $\tilde{\mu}_A$, *ALR*, Ma, Re, We, and *MFR*. The A and B coefficients were determined simultaneously by using the GlobalSearch algorithm in Matlab, based on the *SCA*–p_g results at various T_L and liquids. Since $\tilde{\rho}_L$ was the best-performing non-dimensional number for N_1, the candidates for N_2 are presented in Table 2 by fixing N_1 at $\tilde{\rho}_L$. In addition to R^2, *SSE*, and relative standard deviation of the A constant, $S_{r,A}$, are also presented. Since S_r of B was already low in all the cases, this parameter was omitted from Table 2. By considering only R^2, $\tilde{T}_A$ is the best non-dimensional number candidate for N_2, closely followed by $\tilde{\rho}_A$. However, both of them are characterized by high *SSE* and $S_{r,A}$. Considering all the parameters, *ALR* is the best choice, followed by Ma and *MFR*. The rest of the non-dimensional numbers showed high *SSE* or $S_{r,A}$, hence they are discarded. This latter parameter refers to that even though the fitting of Eq. (19) can be performed by achieving high R^2 values, A varies significantly with the operating condition.

Table 3 summarizes some of the rest combinations which did not work, presenting the results only for D. $N_1 = \tilde{\rho}_L$ was fixed in the first three cases, and then the remaining non-dimensional parameters for N_1 were evaluated with all *ALR*, Ma, and *MFR*, which were performed excellently for N_2, shown in Table 2. Even though high R^2 values could be achieved in several cases, *SSE* and $S_{r,A}$ show that these pairs are inappropriate for *SCA* estimation.

To evaluate the appropriateness of the concluded N_1 and N_2 non-dimensional numbers in Eq. (19), both A and B values were perturbed by 1% in both positive and negative directions while the other one was fixed. The reason behind this was the following. Equation (19), the model, has two variables, while two parameters, T_L and p_g, were varied. Hence, a wide range of N_1 and N_2 can be used with an acceptable fit quality. However, it is expected that the presently approximated and unknown equation for *SCA* determination should not vary much when either A or B constant is slightly altered due to, e.g., measurement error. In other words, a good approximation for *SCA* estimation should show low sensitivity to the model and measurement uncertainties. To quantify this sensitivity, the resulting *SSE* is compared to the original value in percentage, shown in Table 4. The less the increase, the more robust the given form of Eq. (19) is.

It can be concluded that the variation of B has a significantly lower impact on the final result than A. Besides the excellently performing *ALR*, Ma, and *MFR*, $\tilde{T}_A$ was also included since its performance approach that of the other three non-dimensional numbers, even though its original *SSE* was notably higher, shown in Table 2.

Following the ultimate goal of this paper, i.e., determining an empirical correlation that adequately estimates *SCA* of plain-jet airblast atomization in a wide range of conditions, the liquid density ratio, and *ALR* provided the best fit, shown by Eq. (20):

$$SCA = A \cdot \rho_L \cdot ALR^B \tag{20}$$

Here, *ALR* is primarily responsible for describing the variation in p_g. $\tilde{\rho}_L$ incorporates the effect of liquid preheating and is free from the effect of the atomizing air. The liquid-dependent constants in Eq. (20) are summarized in Table 5 for both Ma and *MFR* besides *ALR*. These other two non-dimensional numbers can be used if a fellow researcher would like to extend the validity of Eq. (20) and *ALR* fails to perform well. If Eq. (20) would be the perfect model for *SCA* estimation, then all constants would match. Note that a unified model was tested; however, it was omitted due to the excessive deviation exceeding 100%. The matching of the constants is fulfilled in the case of LHO and RO, which otherwise showed similar behavior in all the previous investigations. However, the exponent of W is largely different, probably due to the very low Oh numbers, which were not achievable by the other liquids. In light of this condition, it is an unexpected result that its *SCA* varied in a similar range than that of LHO and RO. This might change if, e.g., the ambient pressure varies. The physical properties of LHO are close to those of D; however, the generally smaller *SCA* of D resulted in 20% lower A values while B is close to that of LHO and RO. Consequently, the present physical model is not liquid-independent but can be extended by further systematic studies.

Fig. 8 shows the deviation between the measured and estimated *SCA* for all liquids, using Eq. (20). The determined 3.5% maximum deviation is an acceptable result, meaning 1° in *SCA*. The deviation in the experiments of Giffen and Muraszew [30] for a pressure-swirl atomizer was 5%, which is often considered as a reference in the literature of *SCA* estimation. Even though these values could be further reduced by using advanced measurement and evaluation techniques, considering the manufacturing tolerances and the slightly varying conditions in practical systems, this result meets the requirements of common industrial practice.

4. Conclusions

Plain-jet airblast atomization of water (W), diesel oil (D), light heating oil (LHO), and crude rapeseed oil (RO) was investigated in an atmospheric test rig at various atomizing gauge pressures, p_g, and liquid preheating temperatures, T_L. The final goal of this paper was to derive

an empiric equation for the estimation of the spray cone angle, *SCA*. The captured images were processed with an adaptive thresholding algorithm in Matlab software environment to detect the spray edges and ultimately determine *SCA*. To better understand the measurement results, breakup processes in the nearfield of the nozzle were recorded by a high-speed camera. Based on the results, the following conclusions were derived.

1. Eq. (20) estimates *SCA* in the range of the investigated conditions and for all liquids within a 3.5% deviation. Note that the empirical constants in Eq. (20) were varied with the liquid type.
2. Considering the form of Eq. (20), both Ma and *MFR* can reasonably substitute *ALR,* which might be relevant when fellow researchers would like to expand the validity of this *SCA* estimating formula, and *ALR* fails.
3. The variation of T_L is best followed by $\tilde{\rho}_L$, all the other considered non-dimensional numbers containing only liquid properties failed. Even though their R^2 value exceeded 0.9 in several cases, both the relative standard deviation of *A* constant and the sum of squared estimate of errors showed that a small perturbation would make the estimation poor.
4. By evaluating the atomization process in the vicinity of the atomizer nozzle, it can be concluded that D has the greatest jet breakup length that is the reason for low *SCA*. Both D and W are nearly free from ligament formation; the liquid jet breaks up shortly into fine droplets. RO shows intense ligament formation, especially at $T_L = 25$ °C, and short liquid jet breakup. The liquid jet breakup characteristics of LHO lie closely halfway between those of D and RO.
5. By analyzing the variation of the number of white pixels while varying the image threshold, the second local minimum is appropriate for spray edge detection, which gave highly similar results for different shutter speeds.

All the data will be available upon request.

Funding

This paper was supported by the National Research, Development and Innovation Fund of Hungary, project №. OTKA-FK 124704, TUDFO/51757/2019-ITM Thematic Excellence Program, New National Excellence Program of the Ministry for Innovation and Technology, project №. ÚNKP-19–4-BME-213, and the János Bolyai Research Scholarship of the Hungarian Academy of Sciences (Hungarian researchers) and by project No. LTAIN19044 funded from the INTER-EXCELLENCE program by the Ministry of Education, Youth and Sports of the Czech Republic (Czech researchers).

Tilde denotes non-dimensional numbers derived from a single physical quantity.

CRediT authorship contribution statement

András Urbán: Conceptualization, Methodology, Software, Validation, Formal analysis, Investigation, Writing - original draft, Visualization. **Bálint Katona:** Software, Validation, Investigation. **Milan Malý:** Validation, Investigation. **Jan Jedelský:** Resources, Writing - review & editing, Supervision, Funding acquisition. **Viktor Józsa:** Conceptualization, Methodology, Resources, Writing - original draft, Writing - review & editing, Supervision, Project administration, Funding acquisition.

Declaration of Competing Interest

The authors declare that they have no known competing financial interests or personal relationships that could have appeared to influence the work reported in this paper.

References

[1] Martínez-Galván E, Antón R, Ramos JC, Khodabandeh R. Effect of the spray cone angle in the spray cooling with R134a. Exp Therm Fluid Sci 2013;50:127–38. https://doi.org/10.1016/j.expthermflusci.2013.05.012.
[2] Ramana Reddy BV, Mittal R, Maity SR, Pandey KM. Investigation on metallurgical, tribological, hardness properties of spray deposited and warm rolled Al-18Pb, Al-22Pb alloys. J Mater Res Technol 2019;8:5687–97. https://doi.org/10.1016/j.jmrt.2019.09.036.
[3] Zhang P, Su X, Chen H, Geng L, Zhao X. Assessing fuel properties effects of 2,5-dimethylfuran on microscopic and macroscopic characteristics of oxygenated fuel/diesel blends spray. Sci Rep 2020;10:1–12. https://doi.org/10.1038/s41598-020-58119-y.
[4] Lefebvre AH, McDonell VG, Arthur H. Lefebvre VGM. Atomization and Sprays. Second. Boca Raton, FL, FL: CRC Press; 2017.
[5] Raoelison RN, Koithara LL, Costil S, Langlade C. Turbulences of the supersonic gas flow during cold spraying and their negative effects: A DNS CFD analysis coupled with experimental observation and laser impulse high-speed shadowgraphs of the particles in-flight flow. Int J Heat Mass Transf 2020;147:118894https://doi.org/10.1016/j.ijheatmasstransfer.2019.118894.
[6] Vijay GA, Moorthi NSV, Manivannan A. Internal and external flow characteristics of swirl atomizers: A review. At Sprays 2015;25:153–88. https://doi.org/10.1615/AtomizSpr.2014010219.
[7] Chinn JJ. An appraisal of swirl atomizer inviscid flow analysis, part 2: Inviscid spray cone angle analysis and comparison of inviscid methods with experimental results for discharge coefficient, air core radius, and spray cone angle. At Sprays 2009;19:283–308.
[8] Hill H, Ding CP, Baum E, Böhm B, Dreizler A, Peterson B. An application of tomographic PIV to investigate the spray-induced turbulence in a direct-injection engine. Int J Multiph Flow 2019;121:103116https://doi.org/10.1016/j.ijmultiphaseflow.2019.103116.
[9] Hung DLS, Harrington DL, Gandhi AH, Markle LE, Parrish SE, Shakal JS, et al. Gasoline Fuel Injector Spray Measurement and Characterization - A New SAE J2715 Recommended Practice. SAE Int J Fuels Lubr 2008;1:534–5. https://doi.org/10.4271/2008-01-1068.
[10] Warda HA, Kassab SZ, Elshorbagy KA, Elsaadawy EA. An experimental investigation of the near-field region of free turbulent round central and annular jets. Flow Meas Instrum 1999;10:1–14. https://doi.org/10.1016/S0955-5986(98)00042-9.
[11] Maly M, Sapik M, Cejpek O, Wigley G, Katolicky J, Jedelsky J. Effect of spill orifice geometry on spray and control characteristics of spill-return pressure-swirl atomizers. Exp Therm Fluid Sci 2019;106:159–70. https://doi.org/10.1016/j.expthermflusci.2019.04.014.
[12] Jedelsky J, Jicha M. Spatially and Temporally Resolved Distributions of Liquid in an Effervescent Spray. At Sprays 2012;22:603–26. https://doi.org/10.1615/AtomizSpr.2012006055.
[13] Bizjan B, Širok B, Blagojevič M. Experimental investigation of liquid disintegration by twin spinning wheel atomizer. Chem Eng Res Des 2020. https://doi.org/10.1016/j.cherd.2020.02.002.
[14] Meng Y, Zhang Z, Yin H, Ma T. Automatic detection of particle size distribution by image analysis based on local adaptive canny edge detection and modified circular Hough transform. Micron 2018;106:34–41. https://doi.org/10.1016/j.micron.2017.12.002.
[15] Bharodiya AK, Gonsai AM. An improved edge detection algorithm for X-Ray images based on the statistical range. Heliyon 2019;5:e02743https://doi.org/10.1016/j.heliyon.2019.e02743.
[16] Lefebvre AH, Miller D. The Development of an Air Blast Atomizer for Gas Turbine Application. CoA. Report Aero No. 193 June; 1966.
[17] Lasheras JC, Hopfinger EJ. Liquid jet instability and atomization in a coaxial gas stream. Annu Rev Fluid Mech 2000;32:275–308. https://doi.org/10.1146/annurev.fluid.32.1.275.
[18] Ma R, Dong B, Yu Z, Zhang T, Wang Y, Li W. An experimental study on the spray characteristics of the air-blast atomizer. Appl Therm Eng 2015;88:149–56. https://doi.org/10.1016/j.applthermaleng.2014.11.068.
[19] Gad HM, Ibrahim IA, Abdel-baky ME, Abd El-samed AK, Farag TM. Experimental study of diesel fuel atomization performance of air blast atomizer. Exp Therm Fluid Sci 2018;99:211–8. https://doi.org/10.1016/j.expthermflusci.2018.07.006.
[20] Tareq MM, Jung RADS, Lee J. Effect of the Physical Properties of Liquid and ALR on the Spray Characteristics of a Pre-filming Airblast Nozzle. Int J Multiph Flow 2020;126:103240https://doi.org/10.1016/j.ijmultiphaseflow.2020.103240.
[21] Watanawanyoo P, Hirahara H, Mochida H, Furukawa T, Nakamura M, Chaitep S. Experimental investigations on spray characteristics in twin-fluid atomizer. Procedia Eng 2011;24:866–72. https://doi.org/10.1016/j.proeng.2011.12.416.
[22] Charalampous G, Hadjiyiannis C, Hardalupas Y. Comparative measurement of the breakup length of liquid jets in airblast atomisers using optical connectivity, electrical connectivity and shadowgraphy. Meas J Int Meas Confed 2016;89:288–99. https://doi.org/10.1016/j.measurement.2016.03.062.
[23] Pham PX, Kourmatzis A, Masri AR. Local characteristics of fragments in atomizing sprays. Exp Therm Fluid Sci 2018;95:44–51. https://doi.org/10.1016/j.expthermflusci.2018.01.024.
[24] Lay KK, Ang KM, Hung YM, Tan MK. Efficient atomization of brine at atmospheric pressure. J Aerosol Sci 2018;122:11–20. https://doi.org/10.1016/j.jaerosci.2018.05.005.
[25] Lefebvre AH, Arthur H. Lefebvre. Airblast atomization. Prog Energy Combust Sci

1980;6:233–61. doi:10.1016/0360-1285(80)90017-9.
[26] Abramovich GN. The Theory of Turbulent Jets. MIT Press; 1963.
[27] Urbán A, Malý M, Józsa V, Jedelský J. Effect of liquid preheating on high-velocity airblast atomization: From water to crude rapeseed oil. Exp Therm Fluid Sci 2019;102:137–51. https://doi.org/10.1016/j.expthermflusci.2018.11.006.
[28] Faeth GM, Hsiang LP, Wu PK. Structure and breakup properties of sprays. Int J Multiph Flow 1995;21:99–127. https://doi.org/10.1016/0301-9322(95)00059-7.
[29] Chen L, Liu Z, Sun P, Huo W. Formulation of a fuel spray SMD model at atmospheric pressure using Design of Experiments (DoE). Fuel 2015;153:355–60. https://doi.org/10.1016/j.fuel.2015.03.013.
[30] Giffen E., Muraszew A. The atomization of liquid fuels. London Chapman Hall 1953.